

# Benchmarking a trapped-ion quantum computer with 29 algorithmic qubits

Jwo-Sy Chen, Erik Nielsen, Matthew Ebert, Volkan Inlek, Kenneth Wright, Vandiver Chaplin, Andrii Maksymov, Eduardo Páez, Amrit Poudel, Peter Maunz, and John Gamble

IonQ, College Park, MD 20740

Quantum computers are rapidly becoming more capable, with dramatic increases in both qubit count [1] and quality [2]. Among different hardware approaches, trapped-ion quantum processors are a leading technology for quantum computing, with established high-fidelity operations and architectures with promising scaling. Here, we demonstrate and thoroughly benchmark the IonQ Forte system: configured here as a single-chain 30-qubit trapped-ion quantum computer with all-to-all operations. We assess the performance of our quantum computer operation at the component level via direct randomized benchmarking (DRB) across all  $\binom{30}{2} = 435$  gate pairs. We then show the results of application-oriented [3, 4] benchmarks, indicating that the system passes the suite of algorithmic qubit (AQ) benchmarks up to #AQ 29. Finally, we use our component-level benchmarking to build a system-level model to predict the application benchmarking data through direct simulation, including error mitigation. We find that the system-level model correlates well with the observations in many cases, though in some cases out-of-model errors lead to higher predicted performance than is observed. This highlights that as quantum computers move toward larger and higher-quality devices, characterization becomes more challenging, suggesting future work required to push performance further.

## 1 Introduction

The state-of-the-art in quantum computing is rapidly advancing, with researchers actively pursuing multiple promising technology platforms, such as superconducting circuits [5], electronic spins [6], photonics [7], neutral atoms [8], and trapped ions [9]. Currently, the state-of-the-art systems transit the noisy intermediate-scale quantum (NISQ) regime, where contemporary quantum processing units (QPUs) have dozens or hundreds, rather than a handful, of qubits. The level of complexity of these systems presents a variety of challenges, including control system limitations, qubit crosstalk, context dependence and qubit quality uniformity. While it is challenging to maneuver a handful of qubits to high-fidelity operation, it requires significantly more stability and control to orchestrate system-level performance that results in high-fidelity circuit execution across many qubits. For example, the number of distinct gate pairs in an all-to-all connected architecture scales with  $\mathcal{O}(N^2)$ , where  $N$  is the number of qubits in the ion chain, and proportionally increases the difficulty of achieving consistently high performance across all gate pairs.

Along side this challenge is an associated one: how do we judge holistic performance of a many-qubit QPU? One option to qualify user experience is through *application-oriented* benchmarks [4]. These benchmarks, similar to benchmarking suites for classical computing, aim to test performance over a variety of artificial yet realistic problems. Performance on a problem includes classical pre- and post-processing steps such as compiler optimization and error mitigation, allowing refinements in these steps to give higher scores. By ana-

lyzing computer performance over these application benchmarks, we aim to assess quantum computer quality as a user would experience it.

Though application-oriented benchmarks are useful at characterizing user experience, they are not good tools for diagnosing and fixing problems in the QPU hardware. This is because any local problems (*e.g.*, a defective qubit) in application-oriented benchmarks are effectively integrated across an algorithm. For spotting problematic qubits, tuning and initialization, and assessing best-case capability, *component-level* benchmarks, such as randomized benchmarking, are more useful. It is important to note that these component-level benchmarks themselves do not tell the whole story of user experience, and must be taken together with application-oriented benchmarks.

In this work, we connect component-level benchmarks with application-oriented benchmarks. Such connection is a natural extension for holistic characterization, but is non-trivial. Quantum operations can have complex structure in their errors that manifest differently depending on the application being run. We simulate a suite of application benchmarks using a simple model of our QPU constructed from our component-level benchmarking. By comparing the results, we test the extent to which component-level performance can predict the behavior of application-sized circuits.

We apply both component-level and application-oriented benchmarks to a 30-qubit trapped-ion quantum computer. In Forte’s present architecture, all 30 qubits are all-to-all connected in a single, linear ion chain; we present detailed component-level benchmarking of all 435 possible pairs. We show that the system passes at a #AQ 29 level, meaning that we have acceptable (greater than  $1/e$  in circuit Hellinger fidelity [4]) outcomes on a standard corpus of representative volumetric testing circuits out to pre-optimized two-qubit gate counts of  $29^2 = 841$ . This result is possible through a combination of gate quality, compiler optimization, and error mitigation, which we explain in-depth. We use component-level benchmarking to simulate application-oriented benchmarks via a depolarization model of the QPU. Critically, we simulate the entire computation chain comprised of circuit compilation, the quantum gates themselves,

and error mitigation. Overall, we find good agreement between theory and experiment but that the model sometimes predicts higher performance than what is observed in experiment. We note how unmodeled error interacts with error mitigation [10], in circuits that are limiting the #AQ score.

This paper is organized as follows. In Sec. 2 we describe the setup of our system, IonQ Forte, highlighting relevant architecture details. We then provide benchmarking results in Sec. 3, including component-level benchmarks and application-oriented benchmarking. In Sec. 4 we describe the construction of the QPU depolarization model and the circuit simulation of the application-oriented benchmarks, and then compare this simulation to experiment. In Sec. 5 we offer concluding remarks and future outlook.

## 2 Experimental setup

IonQ Forte uses an in-house designed surface linear Paul trap, which consists of separate loading and a quantum operation zones, and, though it is not fundamentally necessary for qubit operations, the traps is housed in a closed-cycle cryostat reaching temperatures below 10 K. Neutral ytterbium atoms are generated via laser ablation, which are then ionized ( $^{171}\text{Yb}^+$ ) via resonant-enhanced multiphoton ionization using lasers at 399 nm and 391 nm and trapped in the loading zone. The ions are transported to the quantum operation zone to form a long chain. In the work presented here, we form a 36-ion chain in the quantum zone by sequential loading, transporting and merging of individually loaded ions. Each chain-loading event typically takes less than 30 minutes and the 36-ion chain generally lasts in the quantum region, ready for information processing, for tens of hours to a few days. We control the trapping electric field such that the center 32 ions are equally spaced by  $3\ \mu\text{m}$  approximately, 30 of which serve as the computational qubits. Similar to Ref. [11], we encode quantum information in the ground-state hyperfine levels,  $|0(1)\rangle \equiv |F = 0(1), m_F = 0\rangle$  of  $^2\text{S}_{1/2}$ , whose preparation, gate operations and read-out are mediated by the dipole allowed transition to the higher energy level  $^2\text{P}_{1/2}$ . All transverse motion in the di-

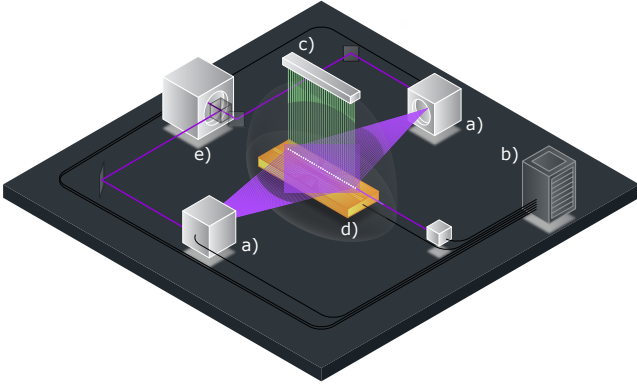


Figure 1: Schematic of IonQ Forte, showing the ion chain axis with respect to addressing Raman beams and imaging. The two AOD devices directing light onto each ion are represented as the objects labeled (a); these devices are controlled by an embedded control system as shown by (b). The ions are imaged onto individual fibers from above as depicted by (c). The ions are held above the surface of a in-house designed surface ion trap (d). The output of Raman source laser (e) is split into the two arms of a counter-propagating beam pair before being modulated by each AOD.

rection parallel to the trap surface in the 36-ion chain is laser-cooled to near the ground state, employing sequential Doppler and EIT cooling [12]. Then, all the ions are optically pumped to the  $|0\rangle$  state before gate operations. To read out the quantum state of qubits, a laser beam resonating with the  $|1\rangle \leftrightarrow |F=0, m_F=0\rangle$  of  $^2P_{1/2}$  transition illuminates the entire ion chain. The photons scattered from each qubit are collected by an in-vacuum high-numerical aperture (NA) lens and directed to an individual multi-mode fiber of a fiber array. Each fiber is attached to a photomultiplier tube (PMT) for photon counting, which allows for simultaneous quantum state read-out of all the ions in the chain. The average state preparation and measurement (SPAM) error is measured to be 0.5% on each qubit across the entire ion chain.

The Fig. 1 depicts a schematic of IonQ Forte which we describe next. To perform quantum gate operations, a pulsed laser at 355 nm is used to drive the two-photon Raman transition between qubit states. Unlike our previously released quantum computers, which utilized multichannel acousto-optic modulators (AOM) and constrained qubit positions to align with the AOM’s beam pitch,

Forte is equipped with four acousto-optic deflectors (AOD) that allow for steering two counter-propagating beam pairs along the trap axis, as shown in Fig. 2, making it possible to independently align each beam to each ion. This degree of freedom allows more flexible trapping potentials [13], leading to smaller beam alignment error across the chain. In addition, the laser focal size can be optimized to balance the beam pointing noise, which is stronger when using a small focal size, with the nearest neighbor cross-talk errors. Using the same laser beam to address different qubits reduces the required average laser power per qubit, which allows the same optical design to access more qubits.

Before each AOD, there is an AOM that provides the necessary control of amplitude, frequency, and phase of each individual laser beam. Each laser beam is focused to approximately  $1.5 \mu\text{m}$  waist along the ion chain axis to realize the individual addressability. Two of four beams paths are designed to be capable of applying an optical phase insensitive single-qubit gate to arbitrary qubits. The four laser beams travel along the quantization axis of the system, set by an applied magnetic field, and are configured to form two counter-propagating beam pairs with perpendicular linear polarizations. Each counter-propagating beam pair can be used to apply an optical phase sensitive single-qubit gate to an arbitrary qubit by steering the beam to its location and setting the laser frequency resonant with the qubit transition. The aforementioned two counter-propagating beam pairs enable the entanglement of arbitrary pairs in the ion chain for the two-qubit gate operations. The current design is capable of addressing 40 ions and  $\binom{40}{2} = 780$  pairs, though the present study uses the 36-ion (30-qubit) configuration due to the number of photon detection channels currently available.

An arbitrary entangling angle two-qubit gate,  $XX_{ij}(\chi)$ , is implemented by the Mølmer-Sørensen scheme using amplitude-modulated pulses [14, 15, 16, 17], where  $i$  and  $j$  are qubit indexes and  $\chi$  represents the angle of entanglement, and  $X$  is the Pauli operator. Each two-qubit gate,  $XX_{ij}(\chi)$ , is surrounded by two  $\pi/2$  single-qubit gates on each side using the same counter-propagating beam pairs for  $XX_{ij}(\chi)$  to form a phase insensitive two-qubit

gate,  $ZZ_{ij}(\chi)$  [18]. The total duration of each single-qubit gate is 110  $\mu\text{s}$ , each of which comprises nine  $\pi/2$  pulses according to the SK1 dynamical correction sequence [19]. The duration of  $ZZ_{ij}(\chi)$  depends on the qubit pair we intend to entangle, and the average duration is about 900  $\mu\text{s}$ .

The quantum computer is managed by a software run-time that automates calibration of native gates and execution of circuits. Circuits in the native SK1 and  $ZZ_{ij}$  representation are executed by an embedded control system that applies a sequence of RF pulses to the AODs and AOMs to perform coherent steering and modulation of the Raman strength. The software run-time maintains optimal pulse parameters through check-and-update cycles interspersed between batches of circuit executions.

To execute an application on the quantum computer a quantum circuit is first submitted through a cloud interface. The quantum circuit is optimized to reduce its gate count (when possible) and compiled to the native gates to match the hardware architecture. Subsequently, it is then downloaded to Forte for execution. Generally, the circuit qubits are re-labelled to the physical qubits, though the component-level benchmarks presented here are in terms of physical qubits.

To reduce the bias in noise accumulation, we use error mitigation by symmetrization [10]. Each circuit is compiled into 25 *variants* that differ by local gate decomposition yet result in the same measurement statistics in the absence of noise. Each variant also has a different circuit-qubit to physical-qubit assignment to further diversify the accumulation of noise. Measurement statistics from each variant implementation is collected and aggregated by plurality voting into a single histogram [10].

### 3 Benchmarking

Benchmarks inform us about how well a quantum computer can be expected to run quantum algorithms. Component-level benchmarks assess the performance of individual pieces (components) of a computer, and by combining these metrics the expected success of an algorithm can be estimated. Application-level or application-oriented benchmarks assess the performance of entire algo-

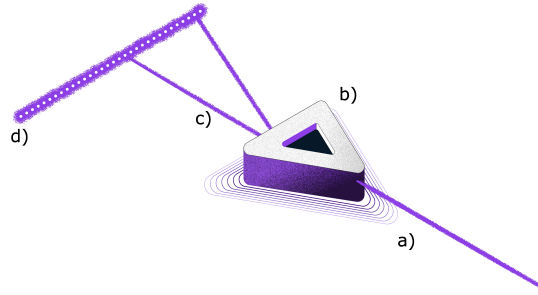


Figure 2: An illustration of the AOD architecture in IonQ Forte. A beam (a) enters the AOD (b) and by modulating the frequency applied to the AOD device an output beam (c) can be directed onto each individual ion (d). Our control system allows for alignment of beams to ions by changing the applied RF tone to the AOD, this allows each ion beam pair to be aligned with a negligible error.

rithms directly.

It may seem that application-oriented benchmarks are then superior, since the process of combining component metrics is not perfect, leaving out types of and interplay between errors that do not show up when testing individual components. This is true when an application of interest coincides exactly with one of the benchmarks, but this is often not the case. Extrapolating performance from one complex algorithm to another, based on similar circuit size for example, is possible but imperfect. Instead, one can estimate performance based on component-level benchmarks (such as gate infidelities). Component-level benchmarks also give us specificity about the location of errors (*e.g.*, a defective qubit), allowing us to fix problems that would be difficult to track down from application-level benchmarks alone. Both types of benchmarks are valuable and contribute to understanding a QPU’s performance. We consider both types separately in the following sections, and then turn to the question of reconciling their predictions.

#### 3.1 Component-level benchmarking

We choose as components the individual single-qubit and two-qubit quantum gates that form circuits and perform direct randomized benchmarking (DRB) [20, 21] on them. The DRB protocol involves selecting circuits by randomly sampling circuit layers according to a chosen distribution. For

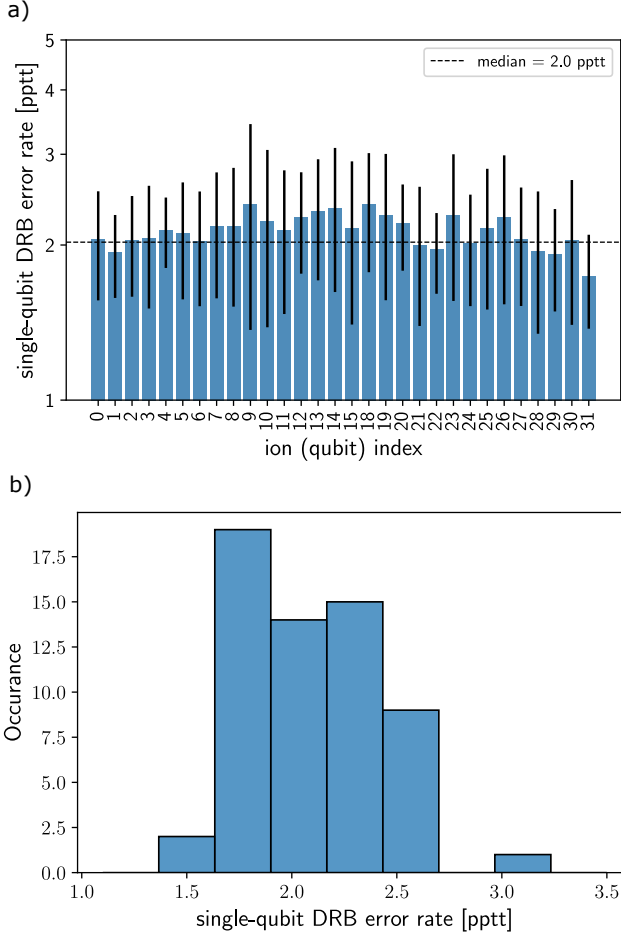


Figure 3: Single-qubit direct randomized benchmarking (DRB) [20] error rate distributions of Forte. Panel (a) shows the error rate per qubit. Error bars give standard deviation across multiple DRB runs on the same qubit, and a black dashed line indicates the median of the per-qubit and -beam-path mean values. The histogram of mean per qubit and beam path error rates is shown in (b). The quantiles in (b) are Median: 2.0 pptt; 10<sup>th</sup> percentile: 1.8 pptt; 90<sup>th</sup> percentile: 2.6 pptt.

each circuit depth  $d$  in a chosen set of circuit depth values,  $N_c$  random circuits are selected. Each random circuit is executed  $N_s$  (a number of samples) times, and then a success probability is computed from the measured outcome frequencies. The decay of average success probability with respect to circuit depth is fit with an exponential decay curve and we extract an error rate measuring the quality of a (random) circuit layer, averaged according to the chosen sampling strategy. In situations where the noise is known or restricted to be purely stochastic, the DRB error rate is equal to the av-

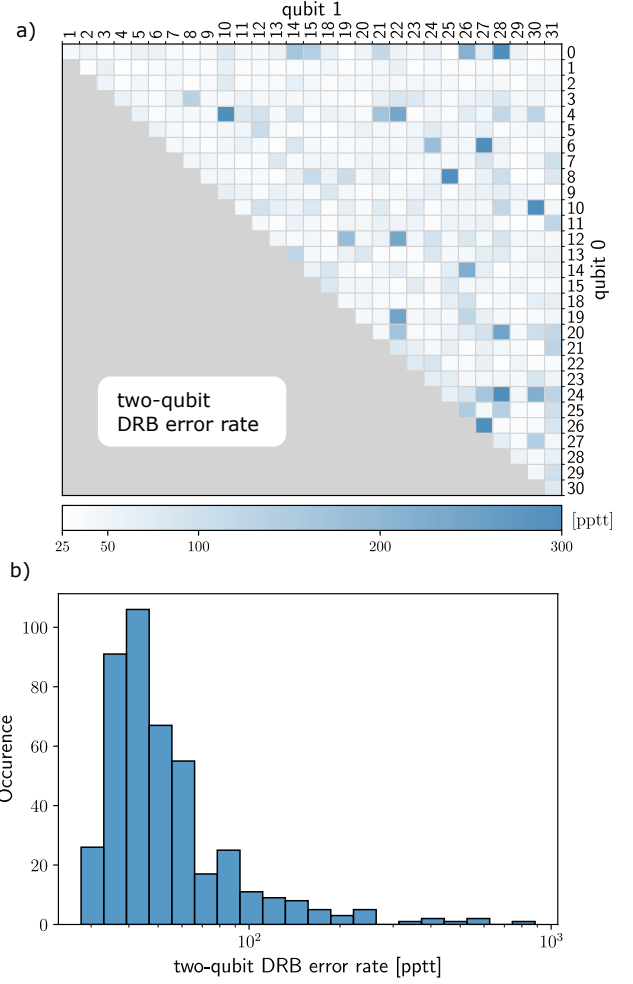


Figure 4: Two-qubit error rates of Forte, measured by direct randomized benchmarking [20]. (a) Mean error rates for each qubit pair. Seven pairs saturate the color scale with error rate  $> 300$ pptt (see supplemental data for precise values). (b) Aggregated mean error rates per pair, with Median: 46.4 pptt; 10<sup>th</sup> percentile: 34.5 pptt; 90<sup>th</sup> percentile: 99.6 pptt, best observed infidelity: 27.8 pptt. Note the logarithmic x-axis scale means a confidence interval of the DRB error rate is visually wider for smaller error rate values.

erage entanglement infidelity of a circuit layer [21]. We perform DRB using its implementation in the `pygsti` software package [22].

DRB on single qubits is performed using parameters  $N_c = 4$ ,  $d \in \{1, 10, 100, 1000\}$ , and  $N_s = 100$ . The gate set is taken to consist of  $x$ - and  $y$ -axis  $\pi/2$ -rotation gates which occur with equal probability. DRB is run on each qubit at least four times, and Fig. 3 presents the obtained values. Fig. 3a plots

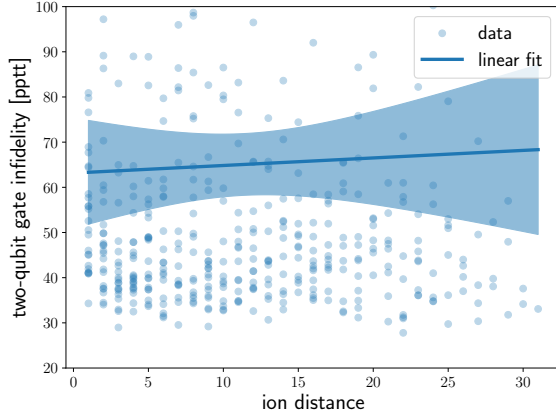


Figure 5: Two-qubit DRB error rate with respect to the ion distance in units of the neighboring ion spacing  $3 \mu\text{m}$ . A linear model is fit to the data to estimate the correlation and the shaded region represents  $2\sigma$  confidence of fit. Although the plot only shows infidelities less than 100 pptt, all the data are included in the fitting. The slope 0.17(45) indicates no statistical significance between infidelity and ion distance.

the error rates for each qubit, with error bars indicating the standard deviation (spread) in the  $\geq 4$  repetitions on the same ion. The histogram of mean per-qubit rates in Fig. 3b shows that the error rates are nicely centered about their median value of 2.0 parts per ten thousand (pptt or  $\times 10^{-4}$ ).

Benchmarking a pair of qubits performs two instances of DRB, each with parameters  $N_c = 4$ ,  $d \in \{1, 5, 22, 100\}$ , and  $N_s = 100$ . Random circuit layers are chosen by selecting the two-qubit gate ( $XX_{ij}$ ) with probability  $p_{2Q}$  or a random pair of single qubit gates with probability  $(1 - p_{2Q})$ . The two instances correspond to  $p_{2Q} = 0.25$  and  $0.75$  respectively. This allows us to extract from the two decay rates independent error rates for the 2-qubit and 1-qubit layers. DRB is run on all the pairs and each pair is measured at least 4 times over the span of approximately six months. The mean 2-qubit DRB error rate for each pair is shown in Fig. 4a. While most pairs are in the 35 – 100 pptt range, there are a number of outliers that result in the long tail of the complete histogram (Fig. 4b). This distribution has median equal to 46.4 pptt, and a tail reaching up to a value of 885 pptt for the worst pair.

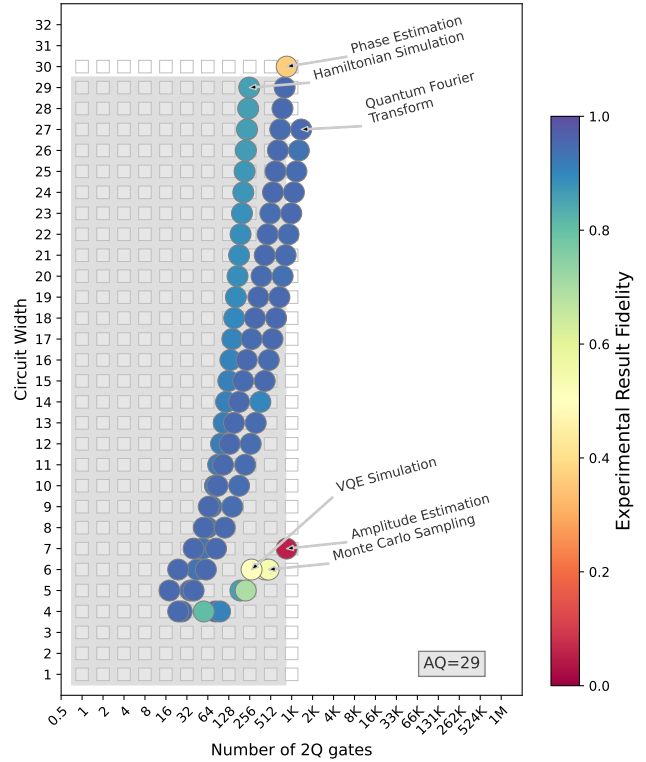


Figure 6: Benchmarking results showing 29 algorithmic qubits on Forte. The x axis is the pre-compilation two-qubit gate counts of the quantum circuits while the y axis represents the circuit width (number of qubits) involved in the quantum algorithms. The data presented here are the minimum fidelity measured in each algorithm.

As the number of ions increases to be large in a single chain, it has been shown that the entangling angle for fixed duration will scale as  $1/r^3$ , where  $r$  is the distance between the two ions in the gate [23]. Similarly, the optimal gate duration should scale with ion distance as spectral crowding of the transverse modes starts to dominate infidelity [24]. In Fig. 5, we plot 2Q DRB error rate versus ion distance and find no statistically meaningful correlation between them. Moreover, we are able to execute gates between any pair with similar laser intensities and durations. This indicates that the above long-chain these effects do not play a role in the present system, suggesting that gate infidelity is not limited, at this time, by chain length.

### 3.2 Application-oriented benchmarking

We measure the number of algorithmic qubits ( $\#AQ$ ) on Forte, an application-oriented benchmark. The  $\#AQ$  benchmark is a modified version of the application-oriented benchmark set forth by the QED-C collaboration [4].  $\#AQ$  is a volumetric benchmark [25] in which six classes of algorithm, corresponding to six practical applications (Hamiltonian simulation, phase estimation, quantum Fourier transform, amplitude estimation, variational quantum eigensolver (VQE) simulation, and Monte Carlo sampling), are run on a quantum computer. Each class of algorithm implements a number of different circuits for each width (number of qubits) of each application. For example, quantum Fourier transform on each distinct width has three different circuits which need to be run successfully to claim a pass for each distinct width. The circuits are provided in a standard form within a QED-C repository [26], and this form is used to define the width  $w_c$  and number of two-qubit gates  $d_c$  of each circuit  $c$ . Note that these values relate to the size of the circuit before any device-specific compilation is performed. The fidelity of  $c$  is defined as [4]

$$F_c = \left( \sum_i \sqrt{p_i q_i} \right)^2, \quad (1)$$

where  $p$  and  $q$  are the measured and ideal outcome probability distributions of  $c$ . A quantum computer has (at least)  $n$  algorithmic qubits when all the circuits in a given set of sample circuits (for all applications) with  $w_c \leq n$  and  $d_c \leq n^2$  run with fidelity  $F_c > 1/e$ . The largest such  $n$  defines the  $\#AQ$  for the computer.

When running the  $\#AQ$  benchmark circuits, 30 physical qubits are used to execute the algorithms. Each circuit is initially generated using the methodology defined in the public QED-C repository [26], and then is submitted to the IonQ cloud via the customer-facing cloud interface. We submit each circuit type for each algorithm width with 2500 shots, where a circuit run is mapped to 25 different variants of that circuit, changing things such as the circuit qubit to physical qubit mapping between variants. Each variant is then executed 100 times and the results are aggregated together via

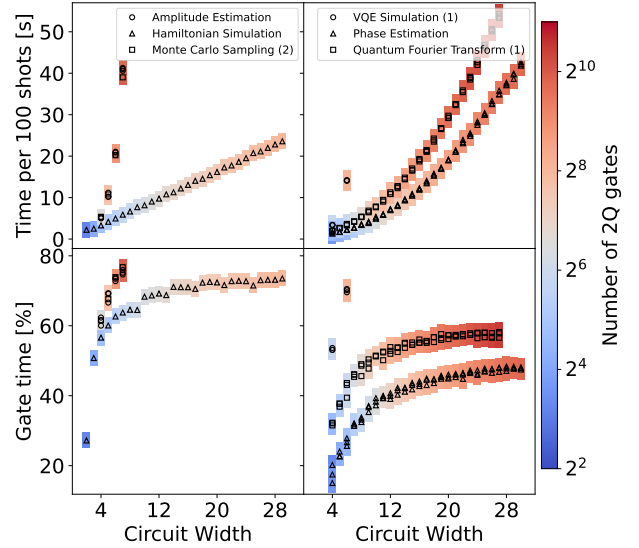


Figure 7: Run timing performance metrics for  $\#AQ$  29 circuits. The top row shows the on-board execution time for 100 shots of each circuit, which *includes* communication between the cloud and the quantum computer, ion cooling, state preparation, quantum circuit execution, state detection, and shot repetition latency. The bottom row shows the fraction of that time actually spent on quantum gates and AOM, AOD switching. Note, overheads from system calibration, circuit compilation, and result processing for error mitigation are excluded.

error mitigation techniques and returned to the end user [10].

The execution time of each variant, which is defined as the duration between when the cloud submits a circuit to Forte and when the cloud receives the computation result from Forte, is summarized in Fig. 7. This includes the classical overhead, such as the communication between the cloud and the quantum computer and shot repetition latency, and the quantum overhead, such as the quantum state preparation and detection, but excludes system calibration, circuit compilation, and data processing occurring in the cloud. The gate time percentage in Fig. 7, which only considers the time spent on the quantum circuit execution, is calculated using the average two-qubit gate time and between-gate padding time that accounts for switching of acousto-optic devices.

Forte achieves  $\#AQ=29$ , which means that all

the circuits falling within the shaded rectangle in Fig. 6 (covering the region  $w_c \leq 29$ ,  $d_c \leq 29^2 = 841$ ) pass the success threshold test stated above. For the work presented here we are limited to #AQ29 by the amplitude estimation class of circuits at circuit width 7 (AE7), highlighting that in general systems tend to be depth not width limited.

## 4 Simulation of the #AQ benchmark

It is natural to ask whether a set of component-level benchmarks, which can be used to estimate the performance of *any* circuit, is consistent with an application-level benchmark. This question has significant practical ramifications, since running application-level benchmarks is 1) less general, in that it targets only a subset of all possible applications and 2) typically much more resource intensive than component-level benchmarks. This second point is especially true as quantum processor (and thereby application) size increases. The first point relates to our understanding of a device: if application-level performance can be accurately predicted based solely on the performance of components, then many of the most insidious types of errors such as crosstalk and context dependence are insignificant.

To address this question we investigate to what extent a depolarizing noise model based on measured DRB error rates (Sec. 3.1) can explain the performance of algorithmic qubit circuits measured in 3.2. By using such a simple noise model we ignore structure in the errors even at the component level, but this is supported by 1) results from gate set tomography (GST) [27] on just a few qubit pairs that indicate the dominant errors are stochastic in nature, and 2) our goal to investigate whether there is a major source of error not accounted for by the individual components, *e.g.*, drift and/or crosstalk errors. For this purpose a depolarizing noise model will suffice, and we defer an error analysis using more detailed error models to future work.

We construct the depolarizing noise model where all single-qubit gates are identical, all two-qubit gates are identical, and the error on each is given by a single depolarization rate  $\epsilon_{1Q}$  and  $\epsilon_{2Q}$  respectively. A depolarization rate  $\epsilon$  on  $n$ -qubit gates

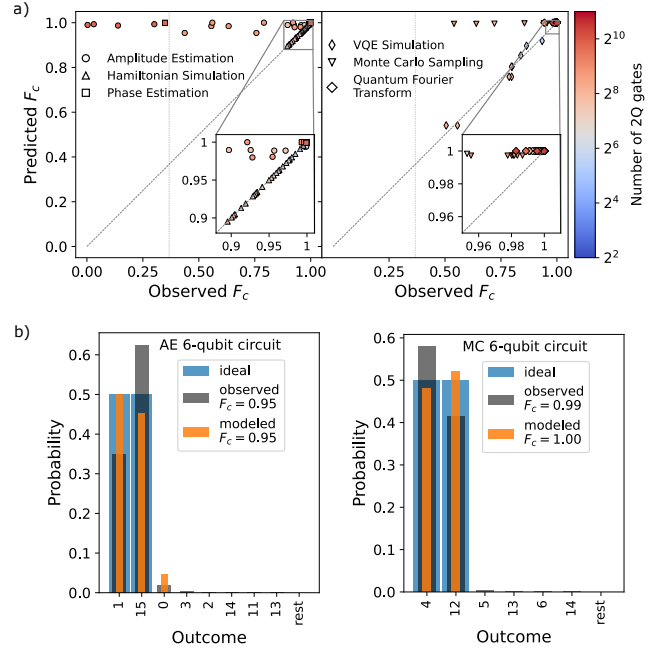


Figure 8: Comparison between simulated and observed outcome application-level benchmarks. (a) Fidelity (Eq. 1) between predicted and ideal vs. observed and ideal circuit outcomes for each of the #AQ circuits executed in Forte. The simulation includes compiler optimization, imperfect qubit operations (via a depolarizing model), and error mitigation. Note that 155/258 of the circuits have both predicted and observed  $F_c = 1$ . (b) Example outcome distribution comparisons for a typical instance of an Amplitude Estimation benchmark on (left) and a Monte Carlo Sampling algorithm (right) on 6 qubits. Bars for the 16 largest outcomes are shown, and remaining outcomes are lumped into a single “rest” entry.

means that noisy gates are modeled as the ideal gate followed by the ( $n$ -qubit) channel

$$\Lambda_\epsilon : \rho \rightarrow (1 - \epsilon)\rho + \frac{\epsilon}{4^n - 1} \sum_{P \neq I} P\rho P, \quad (2)$$

where  $\rho$  is a density matrix, and the sum is over all non-identity tensor products of  $n$  Pauli operations. This definition implies that  $\epsilon_{1Q}$  equals the entanglement infidelity of modeled single-qubit gates and  $\epsilon_{2Q}$  equals the entanglement infidelity of the Molmer-Sorensen gate. We set  $\epsilon_{1Q} = 2.0$  pptt and  $\epsilon_{2Q} = 46.4$  pptt, the median values of the single- and two-qubit DRB error rate distributions, respectively (see Figs. 3b and 4b).

Using this depolarization model, we simulate each of the variant circuits (the final form of the



#AQ circuits that are run on the hardware). Circuits are first compiled to native gates and simulated using Google’s Qsim simulator on a cluster of GPUs with NVIDIA’s cuStateVec back-end library for efficient simulation of the full state vector [28]. The majority-vote aggregation procedure [10] is then applied identically as it is for the experiment.

We show a comparison between the experimental and simulated fidelity (Eq. 1) in Fig. 8 (a). For most circuits where the error mitigation works very well, we find that both the simulation and experiment are near unity. For these cases, we do see out-of-model effects in the raw simulation results, but these discrepancies are corrected by error mitigation. For Hamiltonian Simulation circuits, we find excellent correlation between the experiment and model. This makes intuitive sense, as both the simulation and experiment track the initial state well, which dominates the benchmark comparison. For some Monte Carlo Sampling and Amplitude Estimation circuits, we find that the model matches the ideal distributions with high fidelity, and substantially outperforms the experimental results, indicating the presence of strong unmodeled effects. We show typical histogram results for these cases in Fig. 8 (b).

In Fig. 9, we present the simulation results of the same application-level benchmarks carried out experimentally (Fig. 6), using the identical data analysis procedures as were done in the experiment. We arrive at a predicted #AQ that exceeds the empirical value of 29. The predicted value would equal 30 in this case, its upper limit since both the system and simulation were configured to have 30 physical qubits in this study. In particular, the 7-qubit Amplitude Estimation circuits limiting the performance in the experiment pass the threshold test in the simulated benchmark. This result is not surprising given the tendency of the model to overestimate the performance, as shown in Fig. 8. Inspection of the underlying data suggests that this might be due to an unmodeled coherent error, skewing the distribution of probabilities and leading to an unmitigated bias. For deep circuits, the effect of this bias would become comparable with the decayed signal probability and requires a more precise noise characterization, the subject of ongoing work.

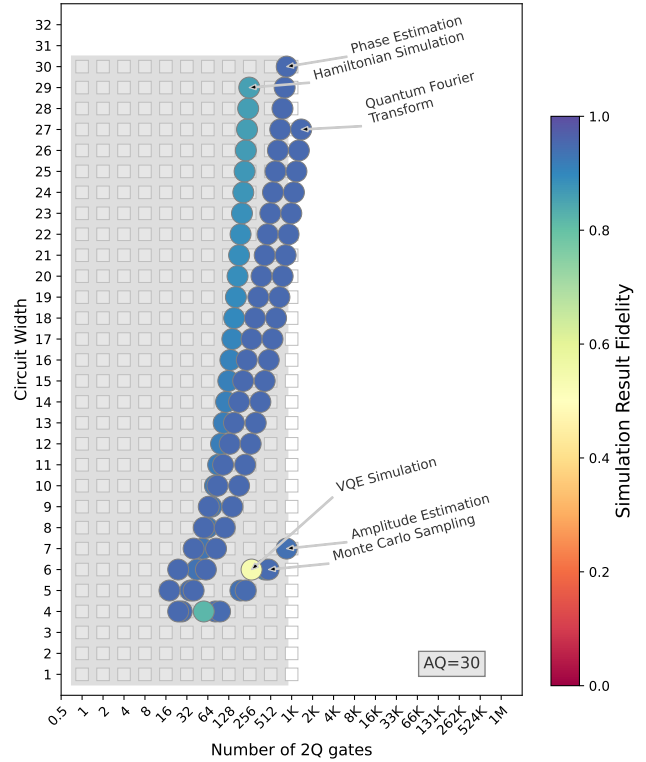


Figure 9: Gate-level simulation of application-oriented benchmarks based on the noise model derived from the characterization data. As with Fig. 6, the x-axis represents two-qubit gate counts in the quantum circuits before compiler optimization, the y-axis represents the circuit width (number of qubits), and the data represent the minimum fidelity reported by simulation.

## 5 Conclusion

In this paper, we showed the operation of an IonQ Forte: a trapped ion quantum computer configured with 30 qubits in a single-linear ion chain. By exhaustively benchmarking all one- and two-qubit gates, we showed that high-fidelity operations are possible, and are not appreciably impacted by ion separation within the chain. To the authors’ knowledge, this demonstrates the longest single-chain trapped ion processor demonstrated to date, showing that performance degradation via long-range interactions does not impact performance at the present scale.

In addition to component benchmarks, we showed a suite of application-level benchmarks passing at the #AQ 29 level. We tracked the runtime and non-gate overhead associated with these

benchmarks, demonstrating that the single-chain architecture allows for both good performance as well as rapid time-to-solution. We ran noisy-gate simulations of application-level benchmarks using a simple model of depolarization rates set by the component-level benchmarks, and including full compiler optimization and error mitigation stack. Despite being simplistic, the model successfully reproduces the experimentally-measured application-level benchmark across most of the circuits in our test suite. However, especially for deep circuits, we observed unmodeled error, which resulted in better predicted performance than what was observed in experiment.

As we strive for cases of useful quantum advantage, we face new and challenging problems stemming from the number of qubits involved and their interactions, rather than their individual basic physics. This is not surprising; Philip Anderson noted fifty years ago that “More is different” [29]. One cannot easily understand psychology by studying the behavior of quarks, and studying how large-scale quantum computer behavior emerges from its components is a daunting task [30]. Indeed, we see that data analysis procedures such as those involved in error mitigation point to important, presently unaccounted-for error mechanisms, and future work is underway to include these observed effects. Further, as quantum computer development continues, engineering them toward reductionism (in which their global behavior can be efficiently decomposed into their constituent parts) will be critical. Toward that end, we see great utility in system-level simulation tools to drive hardware development in this direction, resulting in quantum computers that are not only performant, but also explainable.

## 6 Data availability

All data presented in this paper can be obtained from the supplemental data repository accompanying this work [31]. There, we also include both the pre- and post-compiled circuit variants, raw experimental results, and raw simulation results.

## References

- [1] Youngseok Kim, Andrew Eddins, Sajant Anand, Ken Xuan Wei, Ewout Van Den Berg, Sami Rosenblatt, Hasan Nayfeh, Yantao Wu, Michael Zaletel, Kristan Temme, et al. “Evidence for the utility of quantum computing before fault tolerance”. *Nature* **618**, 500–505 (2023).
- [2] S. A. Moses, C. H. Baldwin, M. S. Allman, R. Ancona, L. Ascarrunz, C. Barnes, J. Bartolotta, B. Bjork, P. Blanchard, M. Bohn, et al. “A race track trapped-ion quantum processor” (2023). [arXiv:2305.03828](https://arxiv.org/abs/2305.03828).
- [3] IonQ. “IonQ Aria Achieves Record 20 Algorithmic Qubits” (2022). (Accessed February 25, 2022).
- [4] Thomas Lubinski, Sonika Johri, Paul Varosy, Jeremiah Coleman, Luning Zhao, Jason Necaie, Charles H. Baldwin, Karl Mayer, and Timothy Proctor. “Application-oriented performance benchmarks for quantum computing”. *IEEE Trans. Quan. Eng.* **4**, 1–32 (2023).
- [5] Morten Kjaergaard, Mollie E Schwartz, Jochen Braumüller, Philip Krantz, Joel I-J Wang, Simon Gustavsson, and William D Oliver. “Superconducting qubits: Current state of play”. *Annu. Rev. Condens. Ma. P.* **11**, 369–395 (2020).
- [6] Guido Burkard, Thaddeus D Ladd, Andrew Pan, John M Nichol, and Jason R Petta. “Semiconductor spin qubits”. *Rev. Mod. Phys.* **95**, 025003 (2023).
- [7] Sergei Slussarenko and Geoff J Pryde. “Photonic quantum information processing: A concise review”. *Appl. Phys. Rev.* **6** (2019).
- [8] Loïc Henriët, Lucas Beguin, Adrien Signoles, Thierry Lahaye, Antoine Browaeys, Georges-Olivier Reymond, and Christophe Jurczak. “Quantum computing with neutral atoms”. *Quantum* **4**, 327 (2020).
- [9] Colin D Bruzewicz, John Chiaverini, Robert McConnell, and Jeremy M Sage. “Trapped-ion quantum computing: Progress and challenges”. *Appl. Phys. Rev.* **6** (2019).

- [10] Andrii Maksymov, Jason Nguyen, Yunseong Nam, and Igor Markov. “Enhancing quantum computer performance via symmetrization” (2023). [arXiv:2301.07233](#).
- [11] K. Wright, K. M. Beck, S. Debnath, J. M. Amini, Y. Nam, N. Grzesiak, J.-S. Chen, N. C. Pisenti, M. Chmielewski, C. Collins, K. M. Hudek, J. Mizrahi, J. D. Wong-Campos, S. Allen, J. Apisdorf, P. Solomon, M. Williams, A. M. Ducore, A. Blinov, S. M. Kreikemeier, V. Chaplin, M. Keesan, C. Monroe, and J. Kim. “Benchmarking an 11-qubit quantum computer”. *Nat. Commun.* **10**, 5464 (2019).
- [12] L. Feng, W. L. Tan, A. De, A. Menon, A. Chu, G. Pagano, and C. Monroe. “Efficient ground-state cooling of large trapped-ion chains with an electromagnetically-induced-transparency tripod scheme”. *Phys. Rev. Lett.* **125**, 053001 (2020).
- [13] J. P. Home, D. Hanneke, J. D. Jost, D. Leibfried, and D. J. Wineland. “Normal modes of trapped ions in the presence of anharmonic trap potentials”. *New Journal of Physics* **13**, 073026 (2011).
- [14] Anders Sørensen and Klaus Mølmer. “Entanglement and quantum computation with ions in thermal motion”. *Phys. Rev. A* **62**, 022311 (2000).
- [15] T. Choi, S. Debnath, T. A. Manning, C. Figgatt, Z.-X. Gong, L.-M. Duan, and C. Monroe. “Optimal quantum control of multimode couplings between trapped ion qubits for scalable entanglement”. *Phys. Rev. Lett.* **112**, 190502 (2014).
- [16] Nikodem Grzesiak, Reinhold Blümel, Kenneth Wright, Kristin M Beck, Neal C Pisenti, Ming Li, Vandiver Chaplin, Jason M Amini, Shantanu Debnath, Jwo-Sy Chen, et al. “Efficient arbitrary simultaneously entangling gates on a trapped-ion quantum computer”. *Nat. Commun.* **11**, 2963 (2020).
- [17] Reinhold Blümel, Nikodem Grzesiak, Neal Pisenti, Kenneth Wright, and Yunseong Nam. “Power-optimal, stabilized entangling gate between trapped-ion qubits”. *npj Quantum Inf.* **7**, 147 (2021).
- [18] Patricia J Lee, Kathy-Anne Brickman, Louis Deslauriers, Paul C Haljan, Lu-Ming Duan, and Christopher Monroe. “Phase control of trapped ion quantum gates”. *J. Opt. B: Quantum and S. O.* **7**, S371 (2005).
- [19] Kenneth R. Brown, Aram W. Harrow, and Isaac L. Chuang. “Arbitrarily accurate composite pulse sequences”. *Phys. Rev. A* **70**, 052318 (2004).
- [20] Timothy J. Proctor, Arnaud Carignan-Dugas, Kenneth Rudinger, Erik Nielsen, Robin Blume-Kohout, and Kevin Young. “Direct randomized benchmarking for multiqubit devices”. *Phy. Rev. Lett.* **123**, 030503 (2019).
- [21] Anthony M. Polloreno, Arnaud Carignan-Dugas, Jordan Hines, Robin Blume-Kohout, Kevin Young, and Timothy Proctor. “A theory of direct randomized benchmarking” (2023). [arXiv:2302.13853](#).
- [22] Erik Nielsen, Kenneth Rudinger, Timothy Proctor, Antonio Russo, Kevin Young, and Robin Blume-Kohout. “Probing quantum processor performance with pygsti”. *Quantum Sci. Technol.* **5**, 044002 (2020).
- [23] K. A. Landsman, Y. Wu, P. H. Leung, D. Zhu, N. M. Linke, K. R. Brown, L. Duan, and C. Monroe. “Two-qubit entangling gates within arbitrarily long chains of trapped ions”. *Phys. Rev. A* **100**, 022332 (2019).
- [24] Yukai Wu, Sheng-Tao Wang, and L.-M. Duan. “Noise analysis for high-fidelity quantum entangling gates in an anharmonic linear paul trap”. *Phys. Rev. A* **97**, 062325 (2018).
- [25] Robin Blume-Kohout and Kevin C. Young. “A volumetric framework for quantum computer benchmarks”. *Quantum* **4**, 362 (2020).
- [26] The Quantum Economic Development Consortium. “QC-app-oriented-benchmarks”. <https://github.com/SRI-International/QC-App-Oriented-Benchmarks> (2021). Accessed: 2023-07-28.
- [27] Erik Nielsen, John King Gamble, Kenneth Rudinger, Travis Scholten, Kevin Young, and

- Robin Blume-Kohout. “Gate set tomography”. *Quantum* **5**, 557 (2021).
- [28] Sergei V. Isakov, Dvir Kafri, Orion Martin, Catherine Vollgraft Heidweiller, Wojciech Mruzekiewicz, Matthew P. Harrigan, Nicholas C. Rubin, Ross Thomson, Michael Broughton, Kevin Kissell, Evan Peters, Erik Gustafson, Andy C. Y Li, Henry Lamm, Gabriel Perdue, Alan K. Ho, Doug Strain, and Sergio Boixo. “Simulations of quantum circuits with approximate noise using qsim and cirq” (2021). [arXiv:2111.02396](https://arxiv.org/abs/2111.02396).
- [29] Philip W. Anderson. “More is different: Broken symmetry and the nature of the hierarchical structure of science.”. *Science* **177**, 393–396 (1972).
- [30] Jordan Hines, Marie Lu, Ravi K Naik, Akel Hashim, Jean-Loup Ville, Brad Mitchell, John Mark Kriekebaum, David I Santiago, Stefan Seritan, Erik Nielsen, et al. “Demonstrating scalable randomized benchmarking of universal gate sets” (2022). [arXiv:2207.07272](https://arxiv.org/abs/2207.07272).
- [31] “Supplemental data for *Benchmarking a trapped-ion quantum computer with 29 algorithmic qubits*.”. [https://github.com/ionq/forte\\_aq29\\_data](https://github.com/ionq/forte_aq29_data) (2023).